Atmospheric Correction at AERONET Locations: A New Science and Validation Data Set

Yujie Wang, Alexei I. Lyapustin, Jeffery L. Privette, Jeffery T. Morisette, and Brent Holben

***Abstract*—This paper describes an Aerosol Robotic Network (AERONET)-based Surface Reflectance Validation Network (ASRVN) and its data set of spectral surface bidirectional reflectance and albedo based on Moderate Resolution Imaging Spectroradiometer (MODIS) TERRA and AQUA data. The ASRVN is an operational data collection and processing system. It receives 50×50 km^2 subsets of MODIS level 1B (L1B) data from MODIS adaptive processing system and AERONET aerosol and water-vapor information. Then, it performs an atmospheric correction (AC) for about 100 AERONET sites based on accurate radiative-transfer theory with complex quality control of the input data. The ASRVN processing software consists of an L1B data gridding algorithm, a new cloud-mask (CM) algorithm based on a time-series analysis, and an AC algorithm using ancillary AERONET aerosol and water-vapor data. The AC is achieved by fitting the MODIS top-of-atmosphere measurements, accumulated for a 16-day interval, with theoretical reflectance parameterized in terms of the coefficients of the Li Sparse–Ross Thick (LSRT) model of the bidirectional reflectance factor (BRF). The ASRVN takes several steps to ensure high quality of results: 1) the filtering of opaque clouds by a CM algorithm; 2) the development of an aerosol filter to filter residual semitransparent and subpixel clouds, as well as cases with high inhomogeneity of aerosols in the processing area; 3) imposing the requirement of the consistency of the new solution with previously retrieved BRF and albedo; 4) rapid adjustment of the 16-day retrieval to the surface changes using the last day of measurements; and 5) development of a seasonal backup spectral BRF database to increase data coverage. The ASRVN provides a gapless or near-gapless coverage for the processing area. The gaps, caused by clouds, are filled most naturally with the latest solution for a given pixel. The ASRVN products include three parameters of the LSRT model (k^L, k^G, and k^V), surface albedo, normalized BRF (computed for a standard viewing geometry, $VZA = 0°, SZA = 45°$), and instantaneous BRF (or one-angle BRF value derived from the last day of MODIS measurement for specific viewing geometry) for the MODIS 500-m bands 1–7. The results are produced daily at a resolution of 1 km in gridded format. We also provide a cloud mask, a quality flag, and a browse bitmap image. The ASRVN data set, including 6 years of MODIS TERRA and 1.5 years of MODIS AQUA data, is available now as a standard MODIS product (MODASRVN) which can be accessed through the Level 1 and Atmosphere Archive and Distribution System website (http://ladsweb.nascom.nasa.gov/data/search.html). It can be used for a wide range of applications including validation analysis and science research.**

***Index Terms*—Aerosols, remote sensing.**

I. Introduction

THE VALIDATION of moderate-resolution (~1 km) surface-reflectance products, including spectral bidirectional reflectance factors (BRFs), albedos, vegetation indexes, and others, is an important component of the Earth Observing System (EOS) [1] and the National Polar Orbiting Environmental Satellite System (NPOESS) programs. Its goal is to establish the accuracy of environmental data products on regional and global scales for a broad range of atmospheric and surface conditions. The EOS program has developed a multilevel strategy with a strong field campaign component [2]–[5]. The field measurements required for *direct* validation analysis provide a detailed and comprehensive look at the local properties, but they usually involve significant resources, are subject to weather uncertainties, and are strongly limited in temporal and spatial coverage. Due to these constraints, recent validation efforts have proposed that product accuracy assessment should also utilize a globally representative sample of sites to complement the direct validation sites [6]. This concept has been endorsed by the Committee on Earth Observing Satellites (CEOS) as the Benchmark Land Multisite Analysis and Intercomparison of Products (BELMANIP) [7].

In this paper, we present an alternative validation approach for moderate resolution global surface-reflectance products over Aerosol Robotic Network (AERONET) sunphotometer sites [8]. The idea is to collect the best ancillary information on atmospheric aerosol and water vapor and perform an independent atmospheric correction (AC) of satellite measurements based on accurate radiative-transfer theory with high-quality control of the input data and results. In the past several years, we have implemented this idea in the AERONET-based Surface Reflectance Validation Network (ASRVN) which is an automated data collection and processing system residing on a dedicated workstation. ASRVN operationally receives the satellite sensors' level 1B (L1B) data (currently the Moderate Resolution Imaging Spectroradiometer (MODIS) TERRA and AQUA from Goddard's MODIS adaptive processing system (MODAPS) and Multiangle Imaging Spectroradiometer (MISR) from Langley's Distributed Active Archive Center) and aerosol and water-vapor information from the AERONET server. After a successful test of data integrity and completeness, ASRVN automatically performs rigorous AC on each sensor's data, creating a sensor-specific record of spectral

Manuscript received September 26, 2008; revised November 19, 2008 and February 2, 2009. First published May 8, 2009; current version published July 23, 2009. The work of A. I. Lyapustin and Y. Wang was supported by NASA EOS Science (Dr. D. Wickland) and NPP (Dr. J. Gleason) Grants.

Y. Wang and A. I. Lyapustin are with the Goddard Earth Sciences and Technology Center, University of Maryland Baltimore County, Baltimore County, MD 21228 USA, and also with the NASA Goddard Space Flight Center, Greenbelt, MD 20771 USA.

J. L. Privette is with the National Climatic Data Center, National Oceanic and Atmospheric Administration Satellite and Information Service, Asheville, NC 28801 USA.

J. T. Morisette is with the U.S. Geological Survey Fort Collins Science Center, Fort Collins, CO 80526-8118 USA.

B. Holben is with the NASA Goddard Space Flight Center, Greenbelt, MD 20771 USA.

Digital Object Identifier 10.1109/TGRS.2009.2016334

U.S. Government work not protected by U.S. copyright.

BRF, albedo, and derivative products (e.g., vegetation index) over more than 100 AERONET sites globally. For each site, products are stored in a gridded format at a 1-km resolution for an area of 50×50 km^2 for MODIS and 32×32 km^2 for MISR. Currently, the ASRVN data set contains 6 years of MODIS TERRA data (since 2000) and 1.5 years of MODIS AQUA data. The AQUA data set will be completed together with MODIS Collection 5 land reprocessing, which produces the MODIS AQUA subsets for the ASRVN.

Many of the ideas implemented in ASRVN originated in the MODIS bidirectional reflectance distribution function (BRDF)/albedo algorithm [9], [10] similarly based on the time-series analysis within 16-day intervals. In this paper, we will be using the term BRF rather than the more commonly used BRDF, which is just a factor of π smaller than BRF.

The ASRVN algorithm for MISR data was presented previously [11]. This paper describes the processing algorithm for MODIS measurements (Sections II and III). Examples of the ASRVN data set are given in Section IV. This paper concludes with a summary.

II. ASRVN Infrastructure

The BRF retrievals from MODIS data use several clear-sky measurements acquired on successive observations of the same area under different viewing geometries. The ASRVN processing starts by gridding the latest MODIS swath data (generated operationally over each AERONET site by the MODAPS production system) and placing the resulting ASRVN Tile in a 16-day processing Queue, which implements a sliding temporal window algorithm. Note that the ASRVN Tile is distinct from the much larger MODIS Land Team's production Tile. Next, it finds a relevant AERONET aerosol and water-vapor record and computes radiative-transfer functions required for AC. After ensuring the quality of input data by filtering clouds and spatially variable aerosols, the ASRVN algorithm performs AC and checks the quality of the final solution. The next three sections will describe preprocessing steps preceding the BRF retrieval.

A. Ancillary Data

AERONET sunphotometers sample the direct solar radiation every 15 min and the diffuse sky radiance over a wide range of angles every 60 min during the daytime. AERONET's automated processing system generates aerosol optical thickness (AOT) and column water vapor from the direct solar measurements. A typical AOT uncertainty for a field instrument is 0.01–0.02 and is spectrally dependent. The inversion algorithm [12] uses almucantar sky measurements to retrieve aerosol microphysical properties (particle size distribution and refractive index) and concentration. AERONET applies several tests to ensure the reliability of retrievals, such as $SZA \geq 45°$ and $AOT_{0.44} \geq 0.4$, and that there were at least 21 independent angles used in each inversion. The tests analyze the sensitivity of retrievals to the single scattering albedo and to the phase function at large scattering angles. These quality assurance (QA) tests significantly reduce the number of complete aerosol characterization records, as compared with the number of AOT records.

The ASRVN algorithm starts with the selection of AERONET aerosol optical thickness and column water-vapor values within 30 min of satellite overpass. If these conditions are met, the algorithm selects the inversion record with aerosol microphysical parameters and size distribution within 2 h of overpass. Otherwise, it uses an aerosol climatology model for a given location derived from multiyear AERONET statistics of reliable retrievals [13]. Because full AERONET inversions are less accurate when aerosol concentration is low, the climatology background aerosol model is always used in our algorithm for clear atmospheric conditions (currently defined as $AOT_{0.44} \leq 0.3$). Our testing and earlier prototyping with MISR data [11] demonstrated that the aerosol climatology significantly improves the stability of the time series of derived surface albedo.

Following the selection of aerosol parameters, the ASRVN algorithm calculates the aerosol optical thickness (AOT_{MIE}), single scattering albedo, and scattering phase function using a lookup table approach [14]. Depending on the AERONET sphericity index, either a spherical (Mie) aerosol model or a model of spheroids is used. The aforementioned calculations provide the spectral dependence of extinction (AOT_{MIE}) in the MODIS wavelengths. However, the AOT from direct solar measurements may differ from AOT_{MIE} for a number of reasons, from the time difference between inversion and direct AOT measurement to uncertainties associated with the AERONET inversion algorithm [15]. For this reason, AOT_{MIE} is further scaled by fitting it to the measured AOT at three AERONET wavelengths (0.44, 0.67, and 0.87 μm). Once the aerosol optical parameters are defined, the radiative-transfer model SHARM [16] calculates the required radiative-transfer functions for the specific water-vapor and spectral response functions of the MODIS TERRA or AQUA instrument using the Interpolation and Profile Correction method [17]. A pixelwise correction for variations of surface elevation (atmospheric pressure) is performed using a spectral interpolation method [18].

B. Implementation of Time-Series Processing

To execute time-series processing (sliding window algorithm), ASRVN first grids MODIS L1B calibrated and geolocated data to a regular 1-km grid. We use the MODIS land gridding algorithm [19] with minor modifications that allow us to better preserve the angular anisotropy of signals in the gridded data when measured reflectance is high, for example, over snow, thick clouds, or water with glint. Next, gridded MODIS data (*Tiles*) are placed in the processing Queue, which can hold up to 16 days of successive measurements. The ASRVN processing uses both individual grid cells, also called pixels in the following sections, and fixed-size (25×25 km^2) areas or blocks required by the cloud-mask (CM) algorithm. In order to organize such processing, we developed a framework of C++ classes and structures (algorithm-specific containers). The class functions are designed to handle processing in the various time-space scales, for example, at the pixel or block level, and for a single (last) day of measurements or all available days in the Queue, or for a subset of days which satisfy certain requirements (filters). The data storage in the Queue is efficiently organized using pointers, which avoids physically moving the previous data in memory when the new data arrive.

The structure of the Queue is shown schematically in Fig. 1. For every day of observations, MODIS measurements are stored as Layers for reflective bands 1–7 and thermal

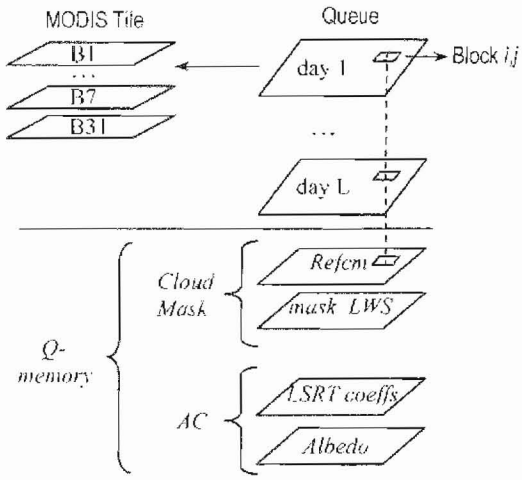

Fig. 1. Structure of the Queue for ASRVN processing. The Queue, designed for the sliding window algorithm, stores up to 16 days of gridded MODIS observations at a 1-km resolution. The CM algorithm uses MODIS bands 1–7 and 31–32, which are stored as Layers (double-indexed arrays) shown in the upper left corner. A dedicated Q-memory is allocated to store the ancillary information for the CM algorithm in *Refcm* structure, such as a reference clear-sky image (*Refcm*) and the results of dynamic land–water–snow classification ($mask_LWS$). This information is updated with latest measurements (day L) once the given block is found cloud free, thus adapting to changing surface conditions. The Q-memory also stores results of previous reliable BRF retrievals, or AC, for MODIS bands 1–7.

bands 31–32, all of which are required by the CM algorithm. Aside from storing gridded MODIS data (*Tiles*), the Queue has a dedicated memory (Q-memory) which accumulates ancillary information about every block and pixel of the surface for the CM algorithm (*Refcm* data structure). It also keeps information related to the history of previous retrievals, such as surface BRF parameters and albedo. Given the daily rate of MODIS observations, the land surface is relatively static over most 16-day periods. Therefore, the knowledge of the previous surface state significantly enhances both the accuracy of the cloud detection and the quality of AC by imposing a requirement of the consistency of the time series of BRF and albedo.

C. Data Quality Control: CM and Aerosol Filter

From the start, ASRVN was designed to work with a multipixel area rather than a single pixel centered at an AERONET location in order to provide optimal visual control over the input and output results. The visual analysis of red–green–blue (RGB) images is superior for complex data quality assessment and troubleshooting situations which is rarely achievable with a pixel (or point)-level analysis.

Although AERONET produces an internal CM [20], it is not sufficient for AC over the 50×50 km^2 processing area. For example, the sunphotometer may provide AOT measurements from a direct sun view through a gap in the clouds. Usually, the sunphotometer's time of measurement differs from satellite overpass time, in which case, changes in cloudiness may have occurred. For these reasons, we implemented a new *multiangle implementation of atmospheric correction (MAIAC)* CM algorithm [21] as part of the ASRVN processing. This algorithm uses the time-series analysis and an image-based rather than pixel-based analysis. It explicitly addresses the problem of cloud searching by identifying a clear-sky comparison target. *MAIAC* CM constructs the reference clear-sky image of the surface and stores it along with other ancillary information about reflectance and brightness temperature for every surface block (25×25 km^2). This ancillary information, required for cloud detection, is continuously updated with the latest cloud-free measurements. This allows the reference image to dynamically adjust to gradual (seasonal) and rapid surface changes caused by snowfall, fires, floods, etc. The CM algorithm is enhanced by an internal dynamic land–water–snow classification, which allows processing flexibility over varying surface types.

Our experience with MODIS data processing dictated the need for additional data screening. This is required when aerosols have significant spatial variation and a single AERONET AOT value does not represent the full processing area, as well as in cases of undetected, usually semitransparent and subpixel, clouds. This screening was implemented through an "aerosol filter." Using the known surface BRF from previous retrievals, the algorithm computes the pixel-level AOT in the blue band from the latest MODIS measurements. The AOT retrieval is a fast algorithm based on a lookup table precalculated for a standard continental aerosol model. The computed AOT is used solely to assess the spatial homogeneity of aerosols over the processing area and to find deviations, which usually indicate previously undetected clouds and sometimes spatially varying aerosols. Specifically, the algorithm generates an AOT histogram from the noncloudy pixels, filters the highest 20% values as possibly cloudy, and finds the average value (AOT_{av}) for the remaining 80% of the pixels. This AOT_{av} is assumed to represent the average clear-sky aerosol loading over the processing area, which should correspond to the AERONET AOT. The AOT_{av} is used next to further filter "suspicious" (contaminated) data as follows. If the atmosphere is clear ($AOT_{\mathrm{av}} < 0.25$), then the algorithm filters only pixels with the high AOT values exceeding the average by 0.15 or more. This threshold was determined through trial and error. Otherwise, it filters the high and low values symmetrically if the difference with AOT_{av} exceeds ± 0.15. This relatively simple technique allows us to filter subpixel clouds, contrails, and other forms of thin cirrus and semitransparent clouds. With the introduction of this additional filter, we witnessed a dramatic enhancement in the quality of the ASRVN AC.

Fig. 2 shows examples of the CM algorithm and aerosol filter for the Goddard Space Flight Center (Greenbelt, MD, U.S.) site. It shows that the CM algorithm captures most of the opaque clouds, whereas the aerosol filter captured additional subpixel and semitransparent clouds and cases of spatially variable aerosols. The example at the bottom of Fig. 2 also shows the detection of cloud shadows by the *MAIAC* CM algorithm. Shadows are detected with a simple threshold algorithm which compares the latest MODIS measurement (ρ^{meas}) with the predicted top-of-atmosphere (TOA) reflectance from the previously retrieved BRF model parameters (ρ^{pred})

$$\mathrm{IF}\ \rho^{\mathrm{meas}} < \rho^{\mathrm{pred}} - 0.12 \Rightarrow \mathrm{CLOUD_SHADOW}.$$

Here, we use a MODIS wavelength of 1.24 μm (band 5) which experiences minimal atmospheric distortions and is usually bright over land so the change of reflectance due to cloud shadow can be easily detected well above the sensor noise level.

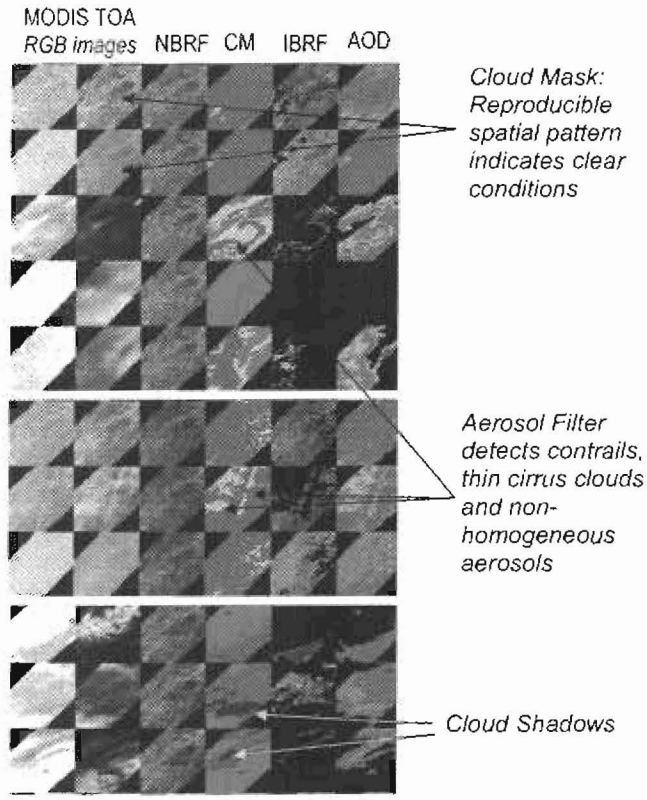

Fig. 2. Example of ASRVN processing for GSFC, U.S., 2006. The two left columns show the TOA gridded RGB MODIS TERRA images for three different sequences of observations. The two left images are differently normalized to help distinguish clouds. The fourth column shows the total generated CM (CM legend: (Blue) Clear, (red) cloud, (yellow) possibly cloud, (dark red) cloud shadow, (gray) aerosol filter). The last column shows the aerosol optical depth (AOD) retrieved from the last day of measurement, which is used in aerosol filter. The AOD is shown using a rainbow palette with pink and red representing the minimum and maximum values, respectively. The third and fifth columns show the results of ASRVN AC (see Section III-C).

III. AC

Once the CM, enhanced by the aerosol filter, is applied, the ASRVN algorithm filters the time series of MODIS measurements for every single pixel and places the remaining good data in a "container." The container stores measurements along with computed Radiative Transfer (RT) functions for the cloud-free days of the Queue. If the number of good measurements exceeds three for a given pixel (see Section III-B), then the coefficients of the Li Sparse–Ross Thick (LSRT) BRF model [22] are computed. The LSRT model is used in the MODIS BRDF/albedo algorithm [9], [10].

A. Inversion for LSRT Coefficients

In the current operational MODIS land processing, the BRF is determined in two steps: First, the AC algorithm derives surface reflectance for a given observation geometry using a Lambertian approximation [23]. Next, three LSRT coefficients are retrieved from the time series of surface reflectance accumulated for a 16-day period [9]. The Lambertian assumption simplifies the AC but imparts biases which depend on observation geometry and atmospheric opacity. Tests show that the Lambertian assumption leads to a more Lambertian BRF shape while the true BRF is more anisotropic [24].

The ASRVN algorithm derives surface LSRT coefficients directly by fitting the radiative-transfer solution to the measured TOA reflectance accumulated over a 4–16-day period. The inversion is based on a high accuracy semianalytical Green's function solution [25], [26], which, in combination with LSRT BRF model, provides an explicit parameterization of TOA reflectance in terms of the surface BRF model parameters $\vec{K} = \{k^L, k^G, k^V\}^{\mathrm{T}}$. According to the derivation provided in the Appendix, the TOA reflectance can be expressed as

$$\begin{aligned} R(\mu_0, \mu, \varphi) = {} & R^D(\mu_0, \mu, \varphi) + k^L F^L(\mu_0, \mu) \\ & + k^G F^G(\mu_0, \mu, \varphi) + k^V F^V(\mu_0, \mu, \varphi) \\ & + R^{\mathrm{nl}}(\mu_0, \mu) \end{aligned} \tag{1}$$

where R^D is the atmospheric (path) reflectance and R^{nl} is a small nonlinear term proportional to the product of the surface and spherical albedos of the atmosphere ($R^{\mathrm{nl}} \propto qc_0$). Functions F^L, F^V, and F^G depend on geometry and atmospheric conditions. They are weakly nonlinear in k-coefficients through the multiple reflection factor $\alpha = (1 - qc_0)^{-1}$.

The quasi-linear form of (1) leads to a very efficient iterative minimization algorithm

$$\begin{aligned} RMSE &= \sum_j \left(r_j^{(n)} - F_j^L k^{L(n)} - F_j^V k^{V(n)} - F_j^G k^{G(n)} \right)^2 \\ &= \min_{\{\vec{K}\}}. \quad r^{(n)} = R - R^D - R^{\mathrm{nl}(n-1)} \end{aligned} \tag{2}$$

where index j denotes the measurements for different days and n is the iteration number. Equation (2) provides an explicit least-squares solution for the kernel weights. In matrix form, the solution is written as

$$\vec{K}^{(n)} = A^{-1} \vec{b}^{(n)} \tag{3}$$

where

$$A = \begin{bmatrix} \sum (F_j^L)^2 & \sum_j F_j^G F_j^L & \sum_j F_j^V F_j^L \\ \sum_j F_j^G F_j^L & \sum_j (F_j^G)^2 & \sum_j F_j^V F_j^G \\ \sum_j F_j^V F_j^L & \sum_j F_j^V F_j^G & \sum_j (F_j^V)^2 \end{bmatrix}$$

$$\vec{b}^{(n)} = \begin{bmatrix} \sum_j r_j^{(n)} F_j^L \\ \sum_j r_j^{(n)} F_j^G \\ \sum_j r_j^{(n)} F_j^V \end{bmatrix}.$$

In the first iteration, the small nonlinear term is set to zero, $R_j^{\mathrm{nl}(0)} = 0$, and the multiple reflection factor α (see the Appendix) is set to one, $\alpha^{(0)} = 1$. These parameters are updated once after the BRF coefficients are calculated in the first iteration. Except for snow-covered surfaces, the problem converges with high accuracy in two iterations because the nonlinear terms are small. Currently, the ASRVN algorithm does not make retrievals over snow.

Prior to inversion, the algorithm checks if the data set has a sufficient angular sampling. The MODIS operational

BRDF/albedo algorithm [9] makes an inversion if at least seven cloud-free observations are available during the 16-day period. We studied this problem experimentally using MODIS data for a number of AERONET sites, varying the minimal required number of measurements (from three to ten) and testing different metrics of angular sampling. One metric used the magnitude of the determinant of the inverse matrix A which shows how different the sampling angles are. Although such analysis is, perhaps, most straightforward theoretically, we found it often too restrictive. In the end, a simple criterion was chosen based on the range of the cosine of the view zenith angle ($\mu_{\max} - \mu_{\min} \geq 0.2$), which ensures robust and consistent retrievals.

The described algorithm [(1)–(3)] has a high computational efficiency. Compared to the radiative-transfer computations, the time required to evaluate functions $F^m(m = L, V, G)$ and R^{nl} is negligible. The integrals required for these functions (see the Appendix) need to be calculated only once regardless of the number of iterations. Finally, small variations of the viewing geometry across the processing area are neglected, and the RT calculation is done once per observation using the geometry of the central pixel of the subset.

B. Solution Selection and Update

Although the LSRT model leads to an efficient BRF retrieval algorithm, there are several caveats associated with this model. The LSRT kernels are not orthogonal, are not positive-only functions, and are normalized in a somewhat arbitrary fashion that is not linked to radiative-transfer theory. These factors reduce the stability and uniqueness of the solutions, such that small perturbations in measurements may lead to significantly different solutions. The high goodness-of-fit at the measurement angles does not guarantee the correct shape of the retrieved BRF and may result in negative BRF values at other angles. The albedo, being an integral function of BRF, is particularly sensitive to an incorrect BRF shape. For these reasons, we developed several tests to remove unrealistic solutions.

The initial validation of the solution (see Fig. 3) checks that the maximal difference over all days of the Queue between measured and computed TOA reflectance does not exceed a specified threshold ($|R^{\mathrm{Meas}} - R^{\mathrm{LSRT}}| > 0.08$). The day (measurement) with the highest deviation is excluded from the Queue, and the inversion is repeated. If the number of measurements goes below four after the exclusion, no retrieval will be made for this pixel.

If a solution provides a good agreement with measurements for all days, the algorithm verifies that values of the direct-beam albedo (q) at $SZA = 15°$, $45°$, and $60°$ are positive. Finally, the new solution must be consistent with the previous solution: $|q(45^o) - q^{\mathrm{Prev}}(45^o)| < \Delta(\lambda)$, where Δ is the band-dependent threshold currently equal to 0.04 (blue), 0.05 (green and red), 0.1 (for the spectral region of 0.8–1.6 μm), and 0.05 for the shortwave infrared band (2.1 μm). The consistency of the time series of BRF and albedo is characterized by a *status* index. Initially, the confidence in the solution is low ($status = 0$). Each time the new retrieval agrees with the previous retrieval, *status* increases by 1. When $status \geq 3$, the retrieval is considered reliable.

The thresholds (0.08 and $\Delta(\lambda)$) in the LSRT inversion routine are selected, on the one hand, tight enough to reject most of undetected clouds, which remain the dominant source of errors, and sufficiently loose, on the other hand, for the solution to adapt to the surface change. The most pervasive type of change is seasonal variations, related to the spring green-up and fall senescence at the northern latitudes or greenness variations caused by wet and dry seasons in the tropics. The total seasonal variation of reflectance (e.g., see Fig. 5) is about several absolute percent in the visible bands and is significantly higher in the near infrared (~0.1–0.2). The ASRVN thresholds for the daily variation are selected accordingly, and our analysis of a large volume of processed MODIS data confirms that the ASRVN algorithm does not reject measurements when the surface is changing, even in the agricultural regions characterized by a rapid reflectance change during harvesting.

When the new solution is validated, the coefficients of the BRF model and direct-beam albedo $q(45°)$, stored in the Q-memory, are updated. The update is done with relaxation, designed to mitigate random noise of retrievals

$$\vec{K}_\lambda^{\mathrm{New}} = \left(\vec{K}_\lambda^{\mathrm{New}} + \vec{K}_\lambda^{\mathrm{Prev}}\right)/2. \tag{4}$$

This method of update increases the quality of the BRF and albedo product when the surface is relatively stable, but it delays the response of the solution to surface changes.

Often, the solution for some pixels or the full area cannot be produced because of the lack of clear-sky measurements. In these cases, we assume that the surface does not change, and we fill in data gaps with the previous solution for up to a 32-day period. In most cases, this assumption of a stable surface is reasonable. The gap-filled pixel is marked as "Extended" in the QA value, with parameter QA.*nDelay* giving the number of days since the last update (see Section III-F).

C. ASRVN Products

The ASRVN computes two main products at a 1-km resolution for seven 500-m MODIS bands, the set of BRF coefficients, and the surface albedo. The albedo is defined by (A5a) as a ratio of surface reflected to incident radiative fluxes. Thus, it represents a true albedo at a given solar zenith angle in ambient atmospheric conditions, the value which can be directly compared to ground-based measurements.

ASRVN also computes several derivative products useful for science data analysis and validation.

1) NBRF—a BRF normalized to the common geometry of nadir view and $SZA = 45°$. This product is analogous to the MODIS nadir BRF-adjusted reflectance product (part of the MOD43 standard product suite). With the geometry variations removed, the time series of NBRF is useful for studying vegetation phenology, performing surface classification, etc.
2) IBRF—an instantaneous (or one-angle) BRF value for the specific viewing geometry of the last day of observations. In essence, IBRF is a reflectance which would be measured if the atmosphere were absent. This product is calculated from the latest MODIS measurement, assuming that the shape of BRF, known from previous retrievals, did not change. To illustrate the computation of

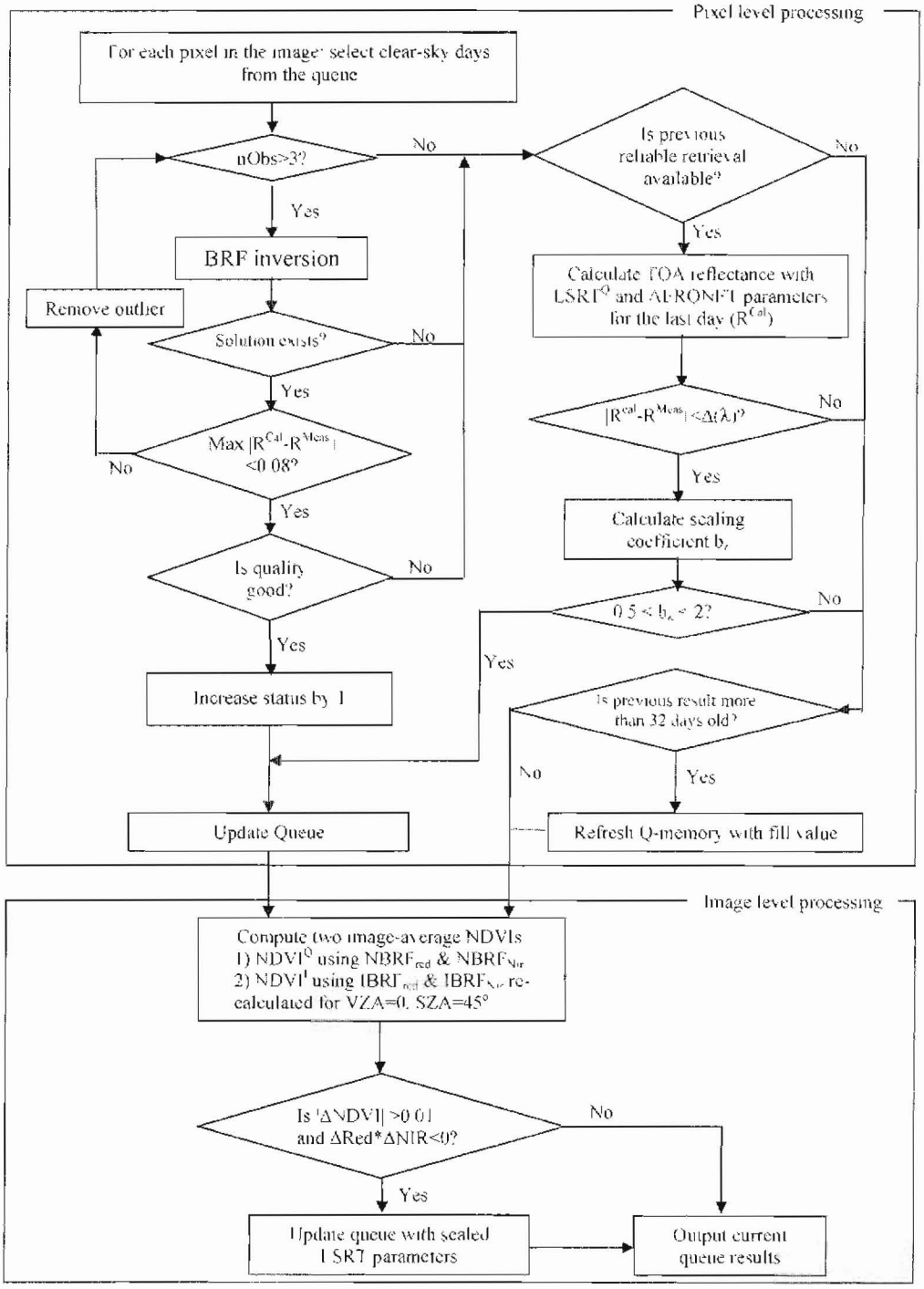

Fig. 3. Block diagram of MODIS AC algorithm.

IBRF, we rewrite (1) for the measured TOA reflectance as follows:

$$R(\mu_0, \mu, \varphi) = R^D(\mu_0, \mu, \varphi) + bR^{\mathrm{Surf}}(\mu_0, \mu, \varphi) \qquad (5)$$

where R^{Surf} combines all surface-related terms and can be calculated using the previous solution for BRF (BRF_λ) and AERONET aerosol information. b is a spectrally dependent scaling factor. Then

$$IBRF_\lambda(\mu_0, \mu, \varphi) = b_\lambda BRF_\lambda(\mu_0, \mu, \varphi). \qquad (6)$$

This algorithm [(6)] will be referred to as scaling. This description was given for the purpose of illustration. In reality, R^{Surf} is a nonlinear function; therefore, computing parameter b_λ and IBRF is done accurately using the formulas given in the Appendix.

The algorithm computing scaling coefficient (and IBRF) is shown in Fig. 3 on the right. First, the algorithm filters measurements which differ from the theoretically predicted TOA reflectance based on the previous solution (R_Q^{LSRT}) by more than a factor of $\Delta(\lambda)$. Then, the scaling coefficients

TABLE I
ASRVN PRODUCT SUITE

Product Name	Data Type	Dimensions	Descriptions	MODIS Product Counterpart
CloudMask	DFNT_UINT8	50x50	Cloud mask field, the definition of values is shown in Table II.	MOD35 cloud Mask
NBRF	DFNT_FLOAT32	50x50x7	Bidirectional reflectance factor normalized to SZA=45° and nadir view	MOD43B4 Nadir BRDF-Adjusted Reflectance (NBAR)
Albedo	DFNT_FLOAT32	50x50x7	Surface albedo at a given solar zenith angle in ambient atmospheric conditions.	A combination of MOD43B3 black-sky and white-sky albedo weighted with respective relative direct and diffuse incident fluxes.
IBRF	DFNT_FLOAT32	50x50x7	Instantaneous (or one-angle) BRF for specific viewing geometry of the last day of observations.	MOD09 Surface reflectance
Kiso	DFNT_FLOAT32	50x50x7	BRF model parameter, the isotropic coefficient.	MOD43B1 BRDF/Albedo Model Parameters
Kvol	DFNT_FLOAT32	50x50x7	BRF model parameter, the volumetric coefficient	MOD43B1 BRDF/Albedo Model Parameters
Kgeo	DFNT_FLOAT32	50x50x7	BRF model parameter, the geometric-optics coefficient.	MOD43B1 BRDF/Albedo Model Parameters
QA	DFNT_UINT16	50x50	Quality assurance flags. The definition of each field can be found in Table III.	N/A
RGB browse image	N/A	50x50	The RGB browse image including TOA reflectance, NBRF, IBRF, CM and QA.	N/A

are computed, and the consistency requirement is verified as $0.5 < b_\lambda < 2$ in the usually dark visible bands and $0.8 < b_\lambda < 1.2$ in the bright near-infrared band. The scaling coefficient's range of variability is roughly consistent with the thresholds for the albedo variations discussed in the previous section. If all conditions are satisfied and the $status$ of the pixel is high ($status \geq 3$), then the LSRT BRF parameters of the pixel stored in the Q-memory are updated with the scaled solution

$$\vec{K}_\lambda^{\text{New}} = \frac{b_\lambda + 1}{2} \vec{K}_\lambda^{\text{Prev}}. \tag{7}$$

Based on its definition, IBRF is well suited for the validation of the surface-reflectance product of the operational atmospheric-correction algorithm (standard product MOD09 [23]).

The CM, the RGB browse images for MODIS TOA reflectance and for the ASRVN NBRF and IBRF, and the QA flag are also standard parts of the ASRVN product suite. The products are saved in hierarchical data format (HDF-EOS) files, which can automatically keep geolocation information and allow data to be ported to virtually any computer platform, regardless of the byte order of the native platform. A list of the ASRVN products and their MODIS product counterparts are given in Table I, and the definition of the CM values is provided in Table II.

TABLE II
CM FIELD DEFINITION

Value	Definition
1	Clear
2	Possibly clear
3	Possibly cloudy
4	Cloudy
5	Cloud shadow
6	"gray" area around cloud pixel, or inhomogeneous aerosol.
10	Clear water
11	Clear snow
12	Clear Land (equivalent to 1)
13	Clear water (equivalent to 10)

D. Update in Case of Rapid Surface Change

Time-series processing is intrinsically controversial when a surface changes rapidly. Since inversions are generally ill-posed problems, one desires all available cloud-free measurements and a maximal time window in order to reduce the $RMSE$. This approach, which reduces the impact of noise in the data (including that of gridding and of residual clouds) and which ensures a more robust BRF shape, is best when the surface is stable throughout the accumulation period. For example, this is the case for natural ecosystems in midlatitudinal summers. In contrast, detecting and tracking surface changes like spring green-up, agricultural harvesting, or fall senescence requires the least possible number of days in the inversion Queue. Such retrievals may have a considerable amount of spatial and spectral noise. Indeed, it is difficult to assess the reliability of solutions when the surface reflectance is changing rapidly or abruptly, particularly given the possibility of data gaps due to clouds.

While the response of the 16-day solution may be delayed, the IBRF tracks spectral changes immediately. The update of Q-memory with the latest measurements by (7) was found to significantly accelerate the response of LSRT coefficients ($\vec{K}_\lambda$) and, hence, of the NBRF, to changing surface conditions. Yet, in some cases, we found this insufficient. To amend results in these cases, we added a separate update of the Q-solution with IBRF based on change detection. This path is shown at the bottom of Fig. 3. Usually, seasonal surface changes related to the vegetation cycle are accompanied by a correlative change in the red-NIR bands, for example, a simultaneous decrease of red and increase of NIR reflectance during green-up and

TABLE III
QA FIELD DEFINITION

Bit field	Bits	Range	Bit-code definition
QA.overall	0-1	00-11	00 - Good quality 01 - acceptable quality 10 – BRF parameters and NBRF are filled with previous results, IBRF is not created 11 – No retrieval is made
QA.scale	2	0-1	0 – Not scaled 1 – scaled
QA.nDelay	3-7	0-31	The number of days since last update of Q-memory
QA.status	8-9	00-11	00 – the BRF consistency parameter *status* =0 01 – *status* =1 10 – *status* =2 11 – *status* >2 (reliable solution)
QA.adjCloud	10	0-1	0 – no adjacent cloud 1 – this pixel is adjacent to a cloudy pixel
QA.model	11	0-1	0 – the calculated IBRF is consistent with the model prediction 1 – the calculated IBRF is not consistent with the model prediction
QA cloud	12	0-1	0 – the pixel is clear 1 – the pixel is cloudy

the opposite changes during fall senescence and defoliation for broadleaf forests. In our case, the change detection is based on the top-of-canopy normalized difference vegetation index (NDVI) [27]. The scene-average NDVI is calculated using the IBRF ($NDVI^I$) and then is normalized to a standard viewing geometry of NBRF. It is compared to the scene-average $NDVI^Q$ calculated using the NBRF stored in the Q-memory (previous reliable solution). A change is defined as when the difference between the two values exceeds ± 0.01. At the same time, the red and NIR reflectance should change accordingly. For example, the following set of rules defines the change during spring green-up:

$$NDVI^I - NDVI^Q > 0.01,\ \rho^I_{\mathrm{Red}} - \rho^Q_{\mathrm{Red}} < 0,\ \rho^I_{\mathrm{NIR}} - \rho^Q_{\mathrm{NIR}} > 0.$$

Such an approach filters fluctuations in NDVI caused by factors unrelated to the vegetation signal, such as residual cloudiness or undetected cloud shadows. Once the change is detected, the Q-memory is updated using (7). Empirically, we found that this approach, which is responsible for 10%–15% of all updates, performs robustly at different global AERONET locations, for example, in North America, Eurasia, or Africa.

The NBRF and albedo are also updated following an update of $\vec{K}_\lambda$ coefficients. This method, which requires only one last day of measurements when the BRF shape is reliably known, is similar to the scheme used in the MODIS BRDF/albedo algorithm [10], and its reliability has been tested with a global composite Advanced Very High Resolution Radiometer (AVHRR) data set [28]. An advantage of this strategy is that, once initialized, the algorithm provides a near gapless coverage and a continuous time series of NBRF and albedo.

Aside from providing a faster response to surface change, the developed update strategy assures fast removal of retrieval artifacts, mainly residual clouds, which is the most common problem.

E. Seasonal Ancillary BRF

When no reliable retrievals are made during the past 32 days, which is usually caused by high cloudiness, the previous retrievals are considered unreliable, and the Q-memory is refreshed with fill values. After that, the algorithm may take a considerable amount of time to reinitialize, during which time, no results will be produced. To remedy this situation, we developed the historical 1-km resolution BRF database from five-year retrievals, which is used for BRF scaling when the Q-memory is being refreshed. This idea of historical backup BRF, providing the angular shape of function, was initially proposed and implemented in the MODIS BRDF/albedo algorithm [10]. The ASRVN BRF database contains one set of spectral k-coefficients for every pixel for each of the four calendar seasons. Initially, the database is built from a multiyear run of ASRVN. The images used for averaging are selected according to the standard deviation of NBRF (σ_{NBRF}) computed for the processing area. Empirically, we found that, with our data QA, the top 20% of images with the highest standard deviation usually contain artifacts from residual clouds or unreliable BRF solutions, whereas the remaining 80% of retrievals have a good quality. Thus, for each site and every season, we first generate the histogram of σ_{NBRF}, find the 80% threshold, and average the images with σ values lower than the threshold.

Once the seasonal BRF database is created, it is supported by an offline background algorithm which updates it with the latest good quality solution.

F. QA Flag

For each execution, the algorithm creates a pixel-level QA flag to indicate the overall quality and the internal processing path. The QA information consists of 16-bit compound bit fields, as summarized in Table III.

The *QA.overall* field indicates the overall data quality. Four values are possible.

1) Good. This means that the *status* of solution is three or greater. In other words, at least three of the last LSRT retrievals agreed, and the calculated IBRF was found to be consistent with the model predictions.
2) Acceptable. In this level, the *status* is not high (≤ 2), but the calculated IBRF agrees with the model prediction.

This case may represent a good solution where only a few retrievals are available because of a gap in AERONET data or clouds.

3) Extended. In this case, either the solution was not produced because of a lack of clear-sky measurements or the calculated IBRF did not agree well with the model prediction. In this case, the previous reliable solution for a given pixel is used to fill in the values of the LSRT coefficients and NBRF. The IBRF in this case is not produced.
4) Not created. This usually happens at the beginning of processing when the Q-memory is not yet initialized.

The field $QA.nDelay$ gives the number of days since the last update of the Q-memory. If $QA.nDelay = 0$, then this pixel contains the most recent retrieval. If the Q-memory was not updated for 32 or more days, the information for a given pixel will be overwritten with the fill value. If the solution is calculated with (7), the *QA.scale* field will be set to one to indicate that the solution is "scaled" from the previous reliable retrieval. The value of the CM for a given pixel is stored in the field *QA.cloud*. We also mask pixels which are adjacent to cloudy pixels, where greater errors in the AC are expected. For such pixels, the *QA.adjCloud* field is set to one (the default value is zero).

IV. Processing Examples

We selected three AERONET sites, Goddard Space Flight Center (GSFC, 38.9925 °N, 76.84 °W), Mongu, Zambia (15.25 °S, 23.15 °E), and Solar Village, Saudi Arabia (24.91 °N, 46.41 °E), to illustrate the ASRVN data set. These sites have very different land cover types, atmospheric conditions, and seasonal variations.

- The GSFC site is located in a northern suburb of Washington, DC. It is a mixture of urban residential area, small deciduous broadleaf forest stands, and small patches of agricultural cropland.
- The Mongu site is located on the eastern side of Zambezi River in western Zambia. The western part of the area is a floodplain mostly covered with grasses, and the eastern part is mainly a sandy soil with sparse vegetation. Significant biomass burning takes place in August and September. In the wet season (November–March), this area has a high cloudiness.
- The Solar Village site is a desert area with stable surface conditions. The dominant aerosol source is dust.

In the following, we provide several examples to demonstrate ASRVN products, data quality, and potential applications. For this study, we exclusively used MODAPS Collection 5 data.

A. NBRF Time Series

The NBRF product has been corrected for both atmospheric effects and variations of view geometry. Thus, NBRF variations should be closely related to changes in surface conditions. Fig. 4 shows the seasonal dynamics of the NBRF images for the three sites. The "true color" images are composed of equal weights from the red, green, and blue spectral bands. The columns show the gridded TOA reflectance, NBRF, and the new CM (the CM legend is given in the figure's caption). Seasonal changes are easy to observe in the first two columns. The vegetative cover reaches a maximum in July–August for the GSFC site, whereas at Mongu, green vegetation is most abundant in January–February, at the height of the wet season. Surface reflectance at the Solar Village site exhibits little variation throughout the year as is expected for a desert location with little vegetation.

To demonstrate the algorithm's performance with different surface types, we selected two pixels for GSFC that differ in the amount of vegetation—a "green" pixel [pixel (16, 36)] in the middle of a small deciduous forest stand to the northeast of the center and a relatively bright "urban" pixel [pixel (46, 3)] representing a typical residential area with mixed vegetation at the lower left corner of the image. For comparison, we also selected a "bright" pixel [pixel (10, 20)] in the desert region of Solar Village. The locations of these pixels are shown by colored circles in Fig. 4. The NBRF time series for these pixels are shown in Fig. 5. For the green pixel, the NBRF in the NIR band increases rapidly during springtime, while the red, green, and blue reflectances decrease. There is an interesting dynamic between the red and green signals. In the early spring, reflectance in the red channel is greater than in the green channel. This is typical of most soils. With the spring green-up, the red band reflectance decreases significantly due to chlorophyll absorption while the change in the green band reflectance is much smaller. During the autumn season, the bands change in the reverse direction as expected for senescing vegetation [Fig. 5(a)]. The urban pixel shows a similar temporal trend, but with much smaller amplitude [Fig. 5(b)]. The time series of the bright pixel at Solar Village does not show much variation throughout the year. The NBRF of band 7 and the NIR, red, green, and blue bands remains around 0.5, 0.42, 0.35, 0.24, and 0.14, respectively. The variation is about $\pm$ 0.03–0.05 in each band.

The data gap in Fig. 5 in year 2004 is due to the incompleteness of the MODIS data set we acquired to date. The remaining gaps will be filled in upon completion of the MODIS land Collection 5 reprocessing, which also generates the MODIS subsets for the AERONET sites for the ASRVN.

B. IBRF Versus NBRF

As discussed in Section III-D, the NBRF, which is retrieved from 4 to 16 days of measurements, may have a delayed response to surface changes. In contrast, the IBRF, derived from the last day of measurements, tracks surface spectral changes immediately. This improvement in temporal sensitivity is sometimes achieved with compromised data quality.

Fig. 6 shows a comparison of NBRF and IBRF for the GSFC site for the spring green-up period (days 95–122) of 2005. There is a seven-day gap in the AERONET records due to cloudiness after day 101. As a consequence, the NBRF and IBRF images show a noticeable color difference on day 108, representing a delayed response of the NBRF to surface change. With the accumulation of six additional measurements, the color of the NBRF and IBRF images become consistent again on day 117. The lag in NBRF depends on the number of available clear-sky measurements and the rate of surface change.

Note that the brightness of the IBRF images in Fig. 6 vary with the view zenith angle. This occurs because the IBRF

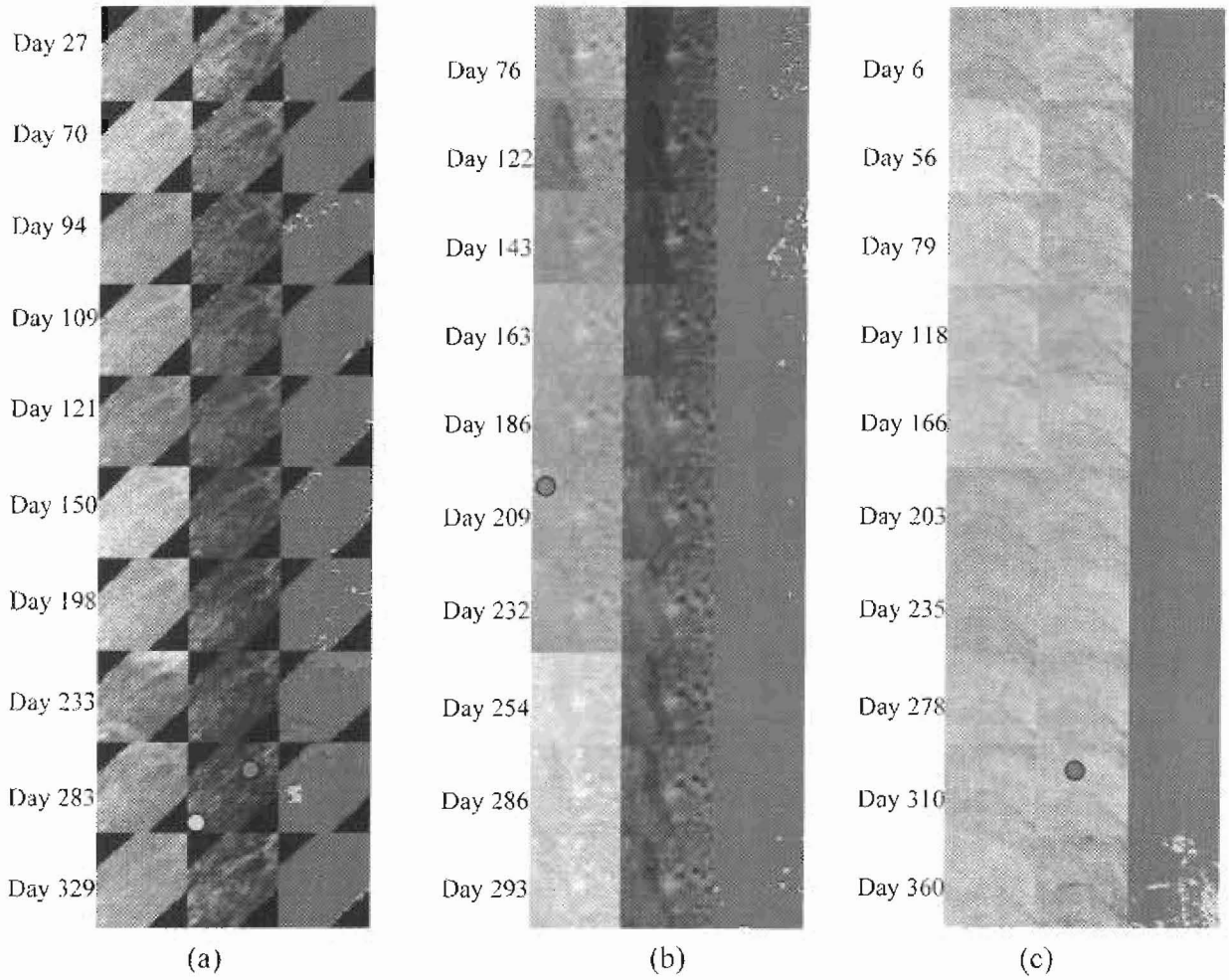

Fig. 4. Temporal dynamics of surface NBRF for (a) GSFC in year 2005, (b) Mongu site in year 2005, and (c) Solar Village site in year 2006. Shown from left to right are the RGB TOA MODIS gridded images, the RGB NBRF images, and the CMs. The true color images are composed from equally weighted red, green, and blue bands. The CM legend is the same as shown in Fig. 2. The red, yellow, and blue dots in panels (a) and (c) show the location of selected green, urban, and bright pixels, respectively. The green dot in panel (b) shows the location of the test pixel in Fig. 7.

images are not normalized, whereas the NBRF images show a stable green-up trend as expected. This confirms that IBRF is more useful for detecting surface changes as well as effects of storms, fires, etc. The more stable NBRF is more suitable for characterizing stable periods, detecting the long-term trends, and support process models, which require low noise of the input data.

To illustrate differences and similarities between NBRF and IBRF quantitatively, we compared the NBRF and $IBRF^N$, normalized to the fixed viewing geometry of NBRF, for the pixel shown by a green circle on the image of the Mongu test site [Fig. 4(b)]. The results for the red and NIR bands are shown in Fig. 7 for 2002–2003. The gaps correspond to the rain seasons with almost continuous cloudiness. The dry season retrievals show a strong seasonal pattern of vegetation superimposed on the signals of soil and drying ponds of flood waters. Compared with $IBRF^N$, the response of NBRF to surface change is delayed by as much as five to eight days. Because cloudiness is very low during the dry season, these NBRF retrievals were obtained with typically 10–16 clear-sky measurements. Fig. 7 also shows a solution obtained with the last four clear-sky measurements. Obviously, the four-day solution shows a much smaller delay (1–2 days) but also a higher noise in the form of several outliers. With higher cloudiness typical of the global performance of ASRVN and with other uncertainties in the input data including the footprint variability, the four-day solution is usually notably noisier than the current solution which uses all clear-sky measurements in the 16-day Queue. The time delay of the NBRF can be removed by comparing it with the time series of $IBRF^N$, which is very similar between the four- and ten-day solutions.

As aforementioned, the variability of footprint with the view angle is the main source of variability of IBRF. To illustrate this point, Fig. 7 shows an $IBRF^N$ averaged over an area of 3×3 pixels (9 km^2), which has a substantially lower noise than the 1-km solution. It is interesting to see that spatial averaging also reduces the temporal bias between $IBRF^N$ and NBRF.

C. NDVI

The NDVI is a commonly used parameter to characterize vegetation canopies. NDVI can be directly derived from the ASRVN BRF and albedo products. NDVI can be generated

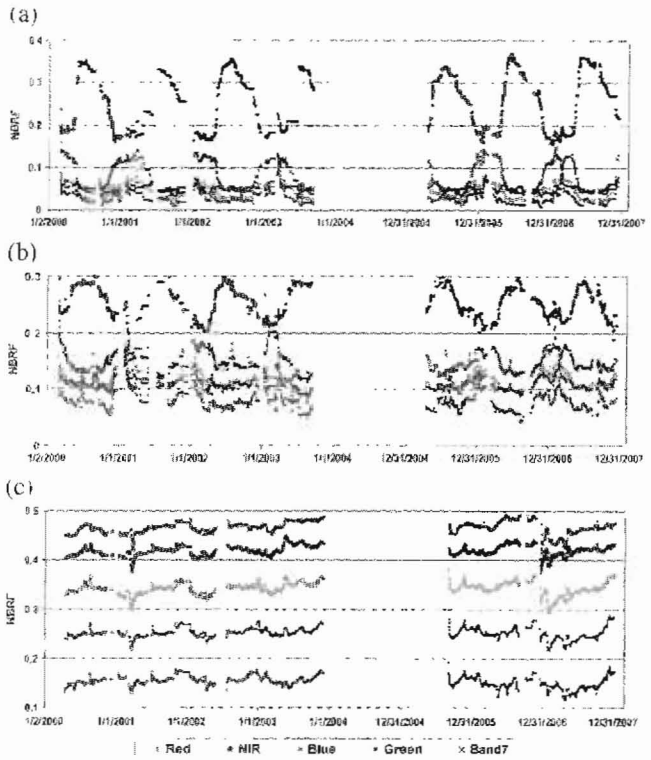

Fig. 5. NBRF time series for (a) green pixel, GSFC site; (b) urban pixel, GSFC site; and (c) bright pixel, Solar village site.

from different reflectance parameters, and its sensitivity to viewing geometry and atmospheric conditions can change accordingly. Fig. 8 shows the NDVI time series for the green and urban pixels of the GSFC site as calculated from NBRF, surface albedo, IBRF (representing different forms of top-of-canopy NDVI), and TOA reflectance. One can see that, in agreement with the expectations, the variation of NDVI derived from NBRF and surface albedo is much smaller than that derived from IBRF and TOA reflectance. The NDVIs derived from the atmospherically corrected products (NBRF, albedo, and IBRF) are also greater than the TOA NDVI. This is expected since AC tends to reduce the red-band reflectance more than the NIR signal. Comparing the NDVIs derived from IBRF and NBRF, we find that the NBRF NDVI generally responds to the seasonal changes with a small delay of several days, with an exception of cases when a larger delay can be traced to a gap in the AERONET data.

D. MODIS Terra Versus Aqua

ASRVN creates a sensor-specific time-series record of the surface reflectance over AERONET sites. Fig. 9 shows the NBRF time series for 1.5 years for the bright pixel of the Solar Village site. The NBRFs are generally very close to each other, which suggests a good relative calibration between the MODIS TERRA and AQUA instruments. The difference may be higher during periods of high cloudiness, when the retrievals are affected by undetected residual clouds and cloud shadows. For example, the maximal NBRF difference for the cloudy period around the end of 2006 is as high as 0.04. For

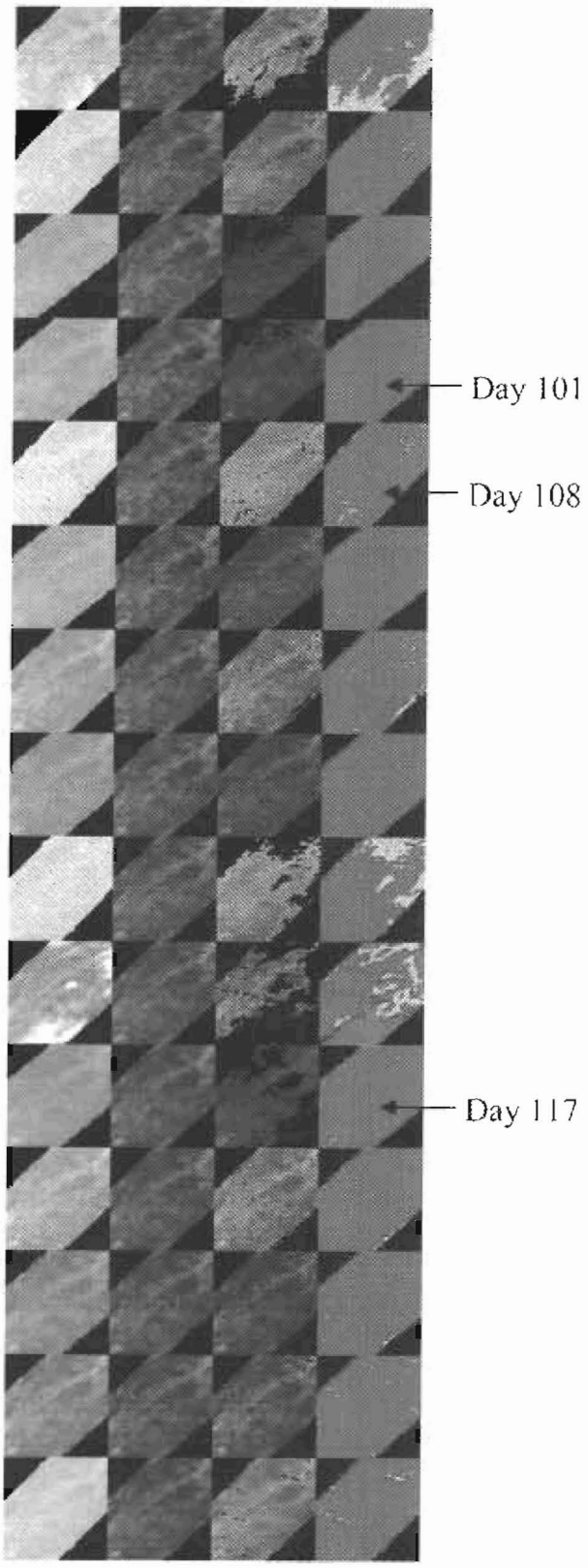

Fig. 6. Comparison of NBRF and IBRF for GSFC, U.S., day 95–122, 2006. Images shown from left to right are the RGB TOA MODIS gridded images, RGB NBRF images, RBG IBRF images, and CM. The CM legend is the same as in Fig. 2.

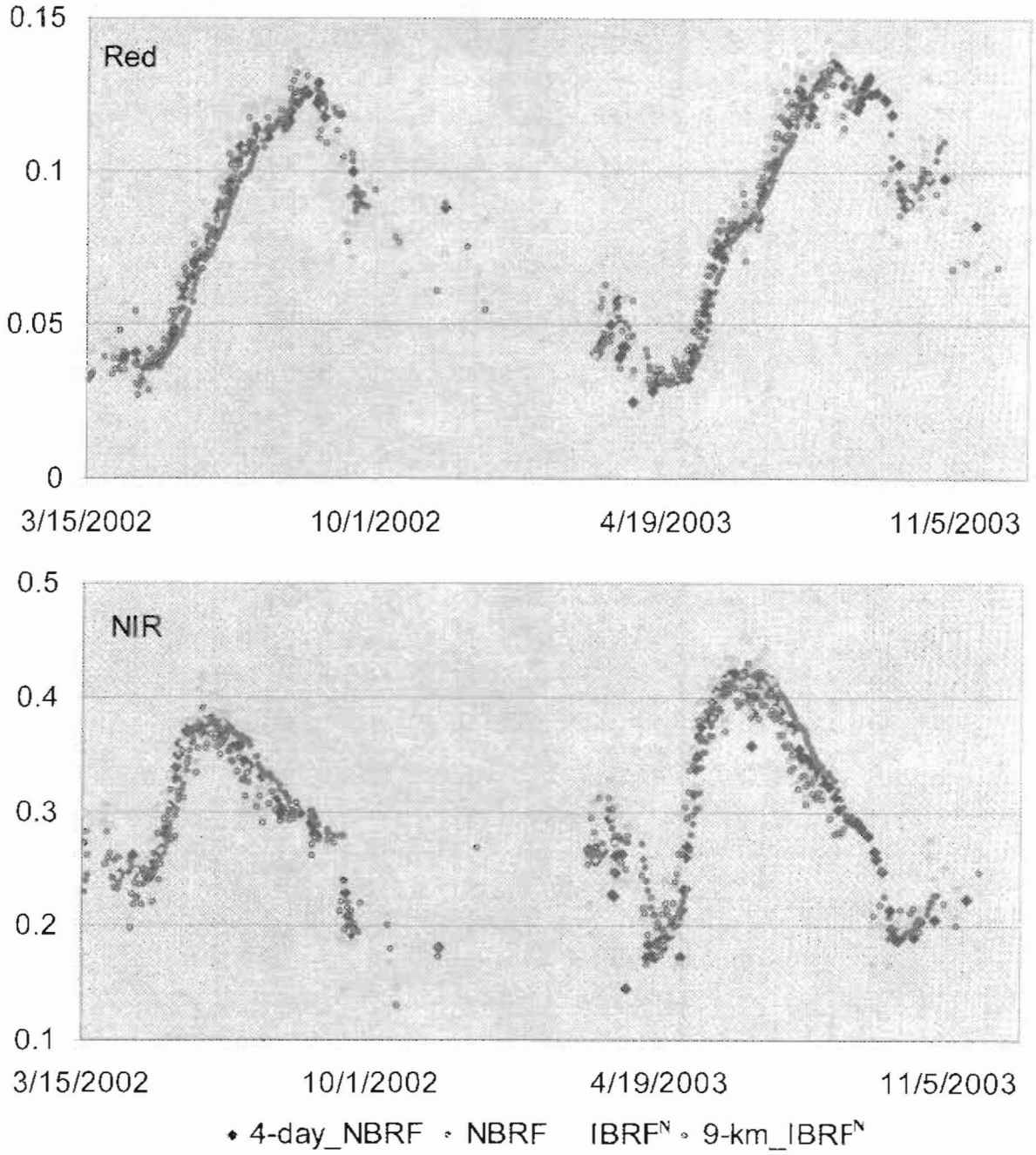

Fig. 7. Comparison of (red) NBRF and (yellow) $IBRF^N$ normalized to the standard viewing geometry of NBRF for the Mongu site for the pixel shown by a green circle in Fig. 4(b). Furthermore, shown is the NBRF obtained from the (green) last four clear-sky days of the Queue and (blue) the $IBRF^N$ averaged over an area of 9 km^2.

the most part, conditions when retrievals are less reliable are captured by the QA flag. For instance, the QA flag indicates lower product quality for about 1.5-month period at the end of 2006 to the beginning of 2007.

Generally, the cross-calibration of sensors flying in different orbits is a very difficult task. With the accumulation of a longer time record and sufficient global statistics, the ASRVN data set may become a valuable source for the cross-calibration analysis of different sensors.

V. Concluding Remarks

This paper has presented a new operational data collection and processing system ASRVN, which was initially designed for the validation of the surface-reflectance products. ASRVN collects MODIS and MISR L1B data for 50×50-km^2 areas for about 160 AERONET sites and performs independent rigorous AC using AERONET aerosol and column water-vapor data. The AC is achieved by fitting 4–16-day (multiangle) sets of MODIS TOA measurements with theoretical reflectance

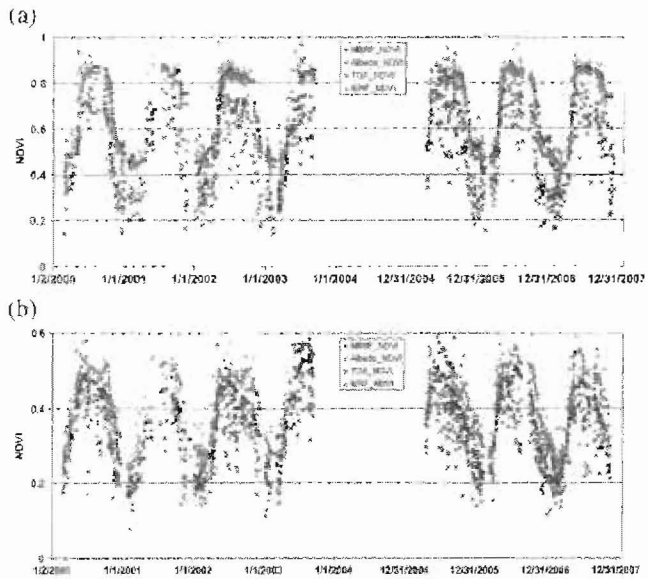

Fig. 8. NDVI time series of (a) green and (b) urban pixels for GSFC site.

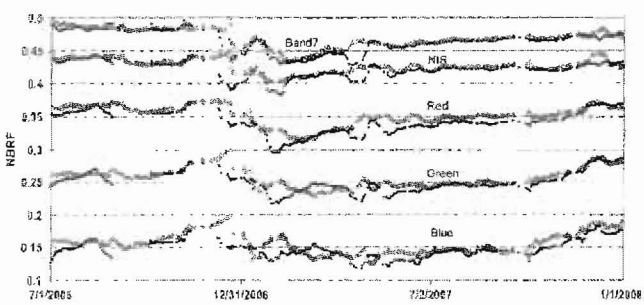

Fig. 9. Comparison of MODIS Terra and Aqua NBRF for a bright pixel (Solar Village). Here, triangles and solid circles represent Aqua and Terra NBRF, respectively.

accurately parameterized in terms of the coefficients of the LSRT BRF model. The algorithm has a thorough data quality analysis component, including a CM, an aerosol filter, and the control of the time-series consistency of surface BRF and albedo.

The algorithm is optimized in terms of noise reduction and its ability to track both seasonal and rapid surface change. During stable surface conditions, such as periods of maximum greenness during summertime in the Northern Hemisphere, a 16-day BRF retrieval gives a solution characterized by low noise. When the surface changes rapidly (e.g., agricultural harvesting), the algorithm gives greater weight to the last MODIS measurement of the period, thus quickly adjusting to the surface change.

We have also developed a backup mechanism to cover extended periods of high cloudiness, when the number of cloud-free MODIS measurements in the 16-day Queue is insufficient for the BRF retrieval. In this case, we use BRF scaling. This approach requires the knowledge of the BRF shape which usually comes from the previous solution stored in the Q-memory. If no retrievals were made in the past 32 days, the algorithm substitutes the Q-solution with the historic seasonal BRF, which represents a quarterly average BRF over years of rettievals. This method allows us to rapidly initialize retrievals after long periods of cloudiness and provide continuous gap-filled imagery of high quality.

The ASRVN suite of products includes three parameters of the LSRT model (k^L, k^G, and k^V), surface spectral albedo, NBRF (a BRF value computed for a standard viewing geometry, $VZA = 0°$, $SZA = 45°$), and IBRF (a BRF value for specific viewing geometry of the last MODIS measurement). All parameters are produced daily for seven 500-m MODIS bands at a gridded 1-km resolution. We do not store vegetation indexes like NDVI which are easy to produce from the available data.

The ASRVN data set, including six years of MODIS TERRA and 1.5 years of MODIS AQUA data, is available now as a standard MODIS product (MODASRVN) which can be accessed through the Level 1 and Atmosphere Archive and Distribution System website (http://ladsweb.nascom.nasa.gov/data/search.html). The products are accompanied by a QA flag and color-composite RGB browse images for the TOA MODIS reflectance, NBRF, IBRF, CM, and QA.

The algorithm has high computational efficiency. For example, a full ASRVN reprocessing of six years of MODIS TERRA data at 100 AERONET sites takes about 24–30 h using one processor of a 2.2-GHz workstation.

The results show very stable and reproducible NBRF and NDVI time series for any given pixel. The main sources of errors in the developed algorithm are the residual cloudiness and the variation of MODIS pixels with scan angle, which increase by a factor of eight from the nadir view to the edge of scan. This effect is partially mitigated by a 1-km resolution gridding procedure, but it cannot be cancelled entirely. This source of uncertainty is important in regions with the high surface heterogeneity at the scale comparable to the grid size of 1 km. In this regard, the expansion of ASRVN with data from the geostationary sensors, such as the future Geostationary Operational Environmental Satellite-R, is expected to produce a higher quality data set.

The ASRVN applications range from product validation and science analysis to sensor calibration support and long-term trending and stability studies. We believe that the products from ASRVN fit well into the CEOS BELMANIP framework and will assist in more reliable and quantitative intercomparison analysis over the AERONET sites. Recently, we conducted a validation study of the MISR surface BRF and albedo products [11]. Because ASRVN produces a multiyear record for each sensor of interest, these data are useful for sensor cross-calibration analysis [30] and detection of long-term calibration trends. The latter are particularly important for climate applications.

The ASRVN prepares a foundation to support the NPOESS validation program for the Visible Infrared Imaging Radiometer Suite (VIIRS) which will replace MODIS and the National Oceanic and Atmospheric Administration's AVHRR as the nation's wide-swath multispectral sensor. The 22-band VIIRS will provide most of the spectral measurements and capabilities afforded by MODIS, with bands highly compatible with the existing ASRVN framework. A constrained pixel growth with the scan angle of the VIIRS as compared to MODIS is an important factor in the data set quality. Because NPOESS is an operational program, validation resources will be significantly more limited than during the EOS era. The NPOESS Validation

Team has defined an initial strategy that strongly emphasizes the use of operational field network data sets (e.g., AERONET + ASRVN) over field campaigns. We envision that, similar to MODIS, the operational processing center will generate VIIRS spatial subsets for ASRVN in near real time. Several targeted postlaunch field campaigns will be undertaken to verify ASRVN results and document performance.

Our approach can be considered as an indirect validation network for current MODIS or MISR surface-reflectance and associated products (e.g., NDVI). If supported by periodic ground measurements over carefully selected stable homogenous test sites with different surface brightness levels, which would establish an absolute reference for BRF and albedo, this approach can also be considered a full validation that is easily expandable to a global level given the AERONET global infrastructure.

APPENDIX

A. Parameterized Expression for the TOA Radiance

The algorithm is based on a high-accuracy semianalytical formula derived with the Green's function method [25], [31]. In the following, τ is the atmospheric optical thickness, πS_λ is the spectral extraterrestrial solar irradiance, and $s = (\mu = \cos\theta, \varphi)$ is a vector of direction defined by zenith (θ) and azimuthal (φ) angles. The z-axis is pointed downward; therefore, $\mu_0 > 0$ for the solar beam, and $\mu < 0$ for the reflected beam. The TOA radiance $L(s_0, s)$ is expressed as a sum of the atmospheric path radiance (D) and surface-reflected radiance (L_s), directly and diffusely transmitted through the atmosphere

$$L(s_0, s) = D(s_0, s) + L_s(s_0, s)e^{-\tau/|\mu|} + L_s^d(s_0, s). \quad \text{(A1)}$$

The surface-reflected radiance is written as

$$L_s(s_0, s) \cong S_\lambda \mu_0 e^{-\tau/\mu_0} \{\rho(s_0, s) + \alpha c_0 \rho_1(\mu)\rho_2(\mu_0)\} + \frac{\alpha}{\pi} \int_{\Omega+} D_s(s_0, s')\rho(s', s)\mu' ds' \quad \text{(A2)}$$

where D_s is the path radiance incident on the surface, c_0 is the spherical albedo of the atmosphere, and

$$\rho_1(\mu) = \frac{1}{2\pi} \int_{\Omega+} \rho(s', s) ds' \qquad \rho_2(\mu_0) = \frac{1}{2\pi} \int_{\Omega-} \rho(s_0, s) ds. \quad \text{(A3)}$$

α is a multiple reflection factor, $\alpha = (1 - q(\mu_0)c_0)^{-1}$, where q is surface albedo. The diffusely transmitted surface-reflected radiance at the TOA is calculated from L_s with the help of the 1-D diffuse Green's function of the atmosphere

$$L_s^d(s_0, s) = \int_{\Omega-} G^d(s_1, s) L_s(s_0, s_1) ds_1. \quad \text{(A4)}$$

The function πG^d is often called bidirectional upward diffuse transmittance of the atmosphere. The method of its calculation was discussed in detail in [23]. The surface albedo is defined as a ratio of reflected and incident radiative fluxes at the surface

$$q(\mu_0) = F^{\mathrm{Up}}(\mu_0)/F^{\mathrm{Down}}(\mu_0) \quad \text{(A5a)}$$

$$F^{\mathrm{Down}}(\mu_0) = \pi S\lambda\mu_0 e^{-\tau/\mu_0} + \int_{\Omega+} D_s(s_0, s')\mu' ds' = F_s^{\mathrm{Dir}}(\mu_0) + F_s^{\mathrm{Dif}}(\mu_0) \quad \text{(A5b)}$$

$$F^{\mathrm{Up}}(\mu_0) = \pi S_\lambda \mu_0 e^{-\tau/\mu_0} q_2(\mu_0) + \int_{\Omega+} \mu' q_2(\mu') D_s(s_0, s')\, ds'$$

$$q_2(\mu_0) = \frac{1}{\pi} \int_{\Omega-} \rho(s_0, s)\mu ds. \quad \text{(A5c)}$$

These formulas give an explicit expression for the TOA radiance as a function of surface BRF. The accuracy of the aforementioned formulas is high, usually within a few tenths of a percent [25]. In the following, we will use the TOA reflectance, which is defined as

$$R_\lambda = L_\lambda/(\mu_0 S_\lambda). \quad \text{(A6)}$$

B. Expression for the TOA Reflectance Using LSRT BRF Model

Based on the described semianalytical solution, we can express the TOA reflectance as an explicit function of parameters of the BRF model. We are using a semiempirical LSRT BRF model [32] as a basis. This is a linear model, represented as a sum of Lambertian, geometric-optical, and volume scattering components

$$\rho(\mu_0, \mu, \varphi) = k^L + k^G f_G(\mu_0, \mu, \varphi) + k^V f_V(\mu_0, \mu, \varphi). \quad \text{(A7)}$$

It uses predefined geometric functions (kernels) f_G and f_V to describe different angular shapes. The kernels are independent of the land conditions. The BRF of a pixel is characterized by a combination of three kernel weights, $\vec{K} = \{k^L, k^G, k^V\}^T$. The LSRT model is used in the operational MODIS BRF/albedo algorithm [9].

The substitution of (A7) into (A1)–(A5) and normalization to the reflectance units gives the following expressions for the surface-reflected signal [the last two terms of (A1)]:

$$R_s(\mu_0, \mu, \varphi) = e^{-\tau/\mu_0}\{k^L + k^G f_G(\mu_0, \mu, \varphi) + k^V f_V(\mu_0, \mu, \varphi) + \alpha c_0 \rho_1(\mu)\rho_2(\mu_0)\} + \alpha\mu_0^{-1}\{k^L E_0^d(\mu_0) + k^G D_G^1(\mu_0, \mu, \varphi) + k^V D_V^1(\mu_0, \mu, \varphi)\} \quad \text{(A8)}$$

$$R_s^d(\mu_0, \mu, \varphi) = e^{-\tau/\mu_0} \times \{[k^L G^{\mathrm{av}}(\mu) + k^G G_G^1(\mu_0, \mu, \varphi) + k^V G_V^1(\mu_0, \mu, \varphi)] + \alpha c_0 [k^L G^{\mathrm{av}}(\mu) + k^G G_G^{11}(\mu) + k^V G_V^{11}(\mu)] \rho_2(\mu_0)\} + \alpha\mu_0^{-1}\{k^L E_0^d(\mu_0) G^{\mathrm{av}}(\mu) + k^G H_G^1(\mu_0, \mu, \varphi) + k^V H_V^1(\mu_0, \mu, \varphi)\}. \quad \text{(A9)}$$

The surface albedo is written as

$$q(\mu_0) = E_0^{-1}(\mu_0)\Big\{\mu_0 e^{-\tau/\mu_0} q_2(\mu_0) + k^L E_0^d(\mu_0) + k^G D_G^3(\mu_0) + k^V D_V^3(\mu_0)\Big\}. \quad \text{(A10)}$$

The different functions of these equations represent different integrals of the incident path radiance (D_s) and atmospheric Green's function (G) with the BRF kernels. They were described in [28] along with the numerical calculation method. In the following, we give only the integral expressions:

$$\rho_1(\mu) = k^L + k^G f_G^1(\mu) + k^V f_V^1(\mu) \quad \text{(A11)}$$

$$\rho_2(\mu_0) = k^L + k^G f_G^2(\mu_0) + k^V f_V^2(\mu_0) \quad \text{(A12)}$$

$$q_2(\mu_0) = k^L + k^G f_G^3(\mu_0) + k^V f_V^3(\mu_0) \quad \text{(A13)}$$

$$D_k^1(\mu_0, \mu, \varphi - \varphi_0) = \frac{1}{\pi}\int_0^1 \mu' d\mu' \int_0^{2\pi} d\varphi' D_s(\mu_0, \mu', \varphi' - \varphi_0) \times f_k(\mu', \mu, \varphi - \varphi') \quad \text{(A14)}$$

$$D_k^3(\mu_0) = \frac{1}{\pi}\int_0^{2\pi} d\varphi' \int_0^1 \mu' f_k^3(\mu') D_s(\mu_0, \mu'; \varphi') d\mu' \quad \text{(A15)}$$

$$G^{\text{av}}(\mu) = \int_{-1}^0 d\mu_1 \int_0^{2\pi} G^d(\mu_1, \mu, \varphi - \varphi_1) d\varphi_1 \quad \text{(A16)}$$

$$G_k^{11}(\mu) = \int_{-1}^0 f_k^1(\mu_1) d\mu_1 \int_0^{2\pi} G^d(\mu_1, \mu, \varphi v - \varphi_1) d\varphi_1 \quad \text{(A17)}$$

$$G_k^1(\mu_0, \mu, \varphi - \varphi_0) = \int_{-1}^0 d\mu_1 \int_0^{2\pi} G^d(\mu_1, \mu, \varphi - \varphi_1) \times f_k(\mu_0, \mu_1, \varphi_1 - \varphi_0) d\varphi_1 \quad \text{(A18)}$$

$$H_k^1(\mu_0, \mu, \varphi - \varphi_0) = \int_{-1}^0 d\mu_1 \int_0^{2\pi} G^d(\mu_1, \mu, \varphi - \varphi_1) \times D_k^1(\mu_0, \mu_1, \varphi_1 - \varphi_0) d\varphi_1. \quad \text{(A19)}$$

The subscript k in the aforementioned expressions refers to either geometric-optical (G) or volumetric (V) kernels, and the supplementary functions of the BRF kernels are given by

$$f_k^1(\mu) = \frac{1}{2\pi}\int_0^1 d\mu' \int_0^{2\pi} f_k(\mu', \mu, \varphi' - \varphi) d\varphi' \quad \text{(A20a)}$$

$$f_k^2(\mu_0) = \frac{1}{2\pi}\int_{-1}^0 d\mu_1 \int_0^{2\pi} f_k(\mu_0, \mu_1, \varphi_1 - \varphi_0) d\varphi_1 \quad \text{(A20b)}$$

$$f_k^3(\mu') = \frac{1}{\pi}\int_{-1}^0 \mu d\mu \int_0^{2\pi} f_k(\mu', \mu, \varphi - \varphi') d\varphi. \quad \text{(A20c)}$$

The diffuse and total spectral surface irradiance are calculated from (A5b) as

$$E_0^d(\mu_0) = F^{\text{Dif}}(\mu_0)/(\pi S_\lambda) \qquad E_0(\mu_0) = F^{\text{Down}}(\mu_0)/(\pi S_\lambda). \quad \text{(A21)}$$

Let us rewrite these equations separating the kernel weights. First, single out small terms proportional to the product $c_0\rho_2(\mu_0)$ into the nonlinear term

$$R^{\text{nl}}(\mu_0, \mu) = \alpha c_0 \rho_2(\mu_0) \times e^{-\tau/\mu_0}\Big\{e^{-\tau/|\mu|}\rho_1(\mu) + k^L G^{\text{av}}(\mu) + k^G G_G^{11}(\mu) + k^V G_V^{11}(\mu)\Big\}. \quad \text{(A22)}$$

Second, collect all remaining multiplicative factors for the kernel weights

$$F^L(\mu_0, \mu) = \Big(e^{-\tau/\mu_0} + \alpha\mu_0^{-1} E_0^d(\mu_0)\Big)\Big(e^{-\tau/|\mu|} + G^{\text{av}}(\mu)\Big) \quad \text{(A23)}$$

$$F^k(\mu_0, \mu; \varphi) = \Big\{e^{-\tau/\mu_0} f_k(\mu_0, \mu, \varphi) + \alpha\mu_0^{-1} D_k^1(\mu_0, \mu, \varphi)\Big\} e^{-\tau/|\mu|} + e^{-\tau/\mu_0} G_k^1(\mu_0, \mu, \varphi) + \alpha\mu_0^{-1} H_k^1(\mu_0, \mu, \varphi), \quad k = V, G. \quad \text{(A24)}$$

With these notations, the TOA reflectance becomes

$$R(\mu_0, \mu, \varphi) = R^D(\mu_0, \mu, \varphi) + k^L F^L(\mu_0, \mu) + k^G F^G(\mu_0, \mu, \varphi) + k^V F^V(\mu_0, \mu, \varphi) + R^{\text{nl}}(\mu_0, \mu). \quad \text{(A25)}$$

This equation, representing the TOA reflectance as an explicit function of the BRF model parameters, provides the means for an efficient AC.

References

[1] M. King and R. Greenstone, *EOS Reference Handbook: A Guide to Earth Science Enterprise and the Earth Observing System*. Greenbelt, MD: EOS Project Sci. Office, NASA/Goddard Space Flight Center, 1999.

[2] J. T. Morisette, J. L. Privette, and C. O. Justice, "A framework for the validation of MODIS land products," *Remote Sens. Environ.*, vol. 83, no. 1/2, pp. 77–96, Nov. 2002.

[3] Y. Wang, C. E. Woodcock, W. Buermann, P. Stenberg, P. Voipio, H. Smolander, T. Häme, Y. Tian, J. Hu, Y. Knyazikhin, and R. B. Myneni, "Evaluation of the MODIS LAI algorithm at a coniferous forest site in Finland," *Remote Sens. Environ.*, vol. 91, no. 1, pp. 114–127, May 2004.

[4] Y. Tian, C. E. Woodcock, Y. Wang, J. L. Privette, N. V. Shabanov, L. Zhou, W. Buermann, J. Dong, B. Veikkanen, T. Hame, M. Ozdogan, Y. Knyazikhin, and R. B. Myneni, "Multiscale analysis and validation of the MODIS LAI product over Maun, Botswana, I. Uncertainty assessment," *Remote Sens. Environ.*, vol. 83, no. 3, pp. 414–430, Dec. 2002.

[5] Y. Tian, C. E. Woodcock, Y. Wang, J. L. Privette, N. V. Shabanov, L. Zhou, W. Buermann, J. Dong, B. Veikkanen, T. Hame, M. Ozdogan, Y. Knyazikhin, and R. B. Myneni, "Multiscale analysis and validation of the MODIS LAI product over Maun, Botswana, II. Sampling strategy," *Remote Sens. Environ.*, vol. 83, no. 3, pp. 431–441, Dec. 2002.

[6] S. Garrigues, R. Lacaze, F. Baret, J. T. Morisette, M. Weiss, J. E. Nickeson, R. Fernandes, S. Plummer, N. V. Shabanov, R. B. Myneni, Y. Knyazikhin, and W. Yang, "Validation and intercomparison of global leaf area index products derived from remote sensing data," *J. Geophys. Res.*, vol. 113, no. G2, p. G02 028, Jun. 2008. DOI: 10.1029/2007JG000635.

[7] F. Baret, J. Morisette, R. Fernandes, J. L. Champeaux, R. Myneni, J. Chen, S. Plummer, M. Weiss, C. Bacour, and G. Derive, "Evaluation of the representativeness of networks of sites for the validation and intercomparison of global land biophysical products: Proposition of the CEOS-BELMANIP," *IEEE Trans. Geosci. Remote Sens.*, vol. 44, no. 7, pp. 1794–1803, Jul. 2006.

[8] B. N. Holben, T. F. Eck, I. Slutsker, D. Tanré, J. P. Bnis, A. Setzer, E. Vermote, J. A. Reagan, Y. J. Kaufman, T. Nakajima, F. Lavenu, I. Jankowiak, and A. Smirnov, "AERONET—A federated instrument network and data archive for aerosol characterization," *Remote Sens. Environ.*, vol. 66, no. 1, pp. 1–16, Oct. 1998.

[9] C. B. Schaaf, F. Gao, A. H. Strahler, W. Lucht, X. Li, T. Tsang, N. C. Strugnell, X. Zhang, Y. Jin, J.-P. Muller, P. Lewis, M. Barnsley, P. Hobson, M. Disney, G. Roberts, M. Dunderdale, C. Doll, R. d'Entremont, B. Hu, S. Liang, and J. L. Privette, "First operational BRDF, Albedo Nadir reflectance products from MODIS," *Remote Sens. Environ.*, vol. 83, no. 1, pp. 135–148, Nov. 2002.

[10] A. H. Strahler and J.-P. Muller, *MODIS BRDF/Albedo Product: Algorithm Theoretical Basis Document*, 1999. NASA EOS-MODIS Doc., Version 5.0.

[11] A. Lyapustin, Y. Wang, J. Martonchik, J. Privette, B. Holben, I. Slutsker, A. Sinyuk, and A. Smirnov, "Local analysis of MISR surface BRF and albedo over GSFC and Mongu AERONET sites," *IEEE Trans. Geosci. Remote Sens.*, vol. 44, no. 7, pp. 1707–1718, Jul. 2006.

[12] O. Dubovik and M. D. King, "A flexible inversion algorithm for retrieval of aerosol optical properties from Sun and sky radiance measurements," *J. Geophys. Res.*, vol. 105, no. D16, pp. 20 673–20 696, 2000.

[13] O. Dubovik, B. Holben, T. F. Eck, A. Smirnov, Y. J. Kaufman, M. D. King, D. Tanre, and I. Slutzker, "Variability of absorption and optical properties of key aerosol types observed in worldwide locations," *J. Atmos. Sci.*, vol. 59, no. 3, pp. 590–608, Feb. 2002.

[14] O. Dubovik, A. Sinyuk, T. Lapyonok, B. N. Holben, M. Mishchenko, P. Yang, T. F. Eck, H. Volten, O. Munoz, B. Veihelmann, W. J. van der Zande, J. Leon, M. Sorokin, and I. Slutsker, "Application of spheroid models to account for aerosol particle nonsphericity in remote sensing of desert dust," *J. Geophys. Res.*, vol. 111, no. D11, p. D11 208, Jun. 2006. DOI: 10.1029/2005JD006619.

[15] O. Dubovik, A. Smirnov, B. N. Holben, M. D. King, Y. J. Kaufman, T. F. Eck, and I. Slutsker, "Accuracy assessments of aerosol optical properties retrieved from AERONET sun and sky-radiance measurements," *J Geophys. Res.*, vol. 105, no. D8, pp. 9791–9806, 2000.

[16] A. I. Lyapustin and T. Z. Muldashev, "Method of spherical harmonics in the radiative transfer problem with non-Lambertian surface," *J. Quant. Spectrosc. Radiat. Transf.*, vol. 61, no. 4, pp. 545–555, Mar. 1999.

[17] A. Lyapustin, "Interpolation and Profile Correction (IPC) method for shortwave radiative transfer in spectral intervals of gaseous absorption," *J. Atmos. Sci.*, vol. 60, no. 6, pp. 865–871, 2003.

[18] R. C. Levy, L. A. Remer, S. Mattoo, E. F. Vermote, and Y. J. Kaufman, "Second-generation operational algorithm: Retrieval of aerosol properties over land from inversion of Moderate Resolution Imaging Spectroradiometer spectral reflectance," *J. Geophys. Res.*, vol. 112, no. D13, p. D13 211, Jul. 2007. DOI: 10.1029/2006JD008711.

[19] R. E. Wolfe, D. P. Roy, and E. Vermote, "MODIS land data storage, gridding, and compositing methodology: Level 2 grid," *IEEE Trans. Geosci. Remote Sens.*, vol. 36, no. 4, pp. 1324–1338, Jul. 1998.

[20] A. Smirnov, B. N. Holben, T. F. Eck, O. Dubovik, and I. Slutsker, "Cloud-screening and quality control algorithms for the AERONET database," *Remote Sens. Environ.*, vol. 73, no. 3, pp. 337–349, Sep. 2000.

[21] A. Lyapustin, Y. Wang, and R. Frey, "An automatic cloud mask algorithm based on time series of MODIS measurements," *J. Geophys. Res.*, vol. 113, no. D16, p. D16 207, Aug. 2007. DOI: 10.1029/2007JD009641.

[22] X. Li and A. H. Strahler, "Geometric-optical bidirectional reflectance modeling of the discrete crown vegetation canopy: Effect of crown shape and mutual shadowing," *IEEE Trans. Geosci. Remote Sens.*, vol. 30, no. 2, pp. 276–292, Mar. 1992.

[23] E. F. Vermote and A. Vermeulen, *Atmospheric Correction Algorithm: Spectral Reflectances (MOD09). Algorithm Theoretical Basis Document*, 1999. NASA EOS-MODIS Doc., Version 4.0.

[24] A. I. Lyapustin, "Atmospheric and geometrical effects on land surface albedo," *J. Geophys. Res.*, vol. 104, no. D4, pp. 4123–4143, 1999.

[25] A. Lyapustin and Y. Knyazikhin, "Green's function method in the radiative transfer problem. I: Homogeneous non-Lambertian surface," *Appl. Opt.*, vol. 40, pp. 3495–3501, 2001.

[26] A. Lyapustin and Y. Knyazikhin, "Green's function method in the radiative transfer problem. II: Spatially heterogeneous anisotropic surface," *Appl. Opt.*, vol. 41, no. 27, pp. 5600–5606, Sep. 2002.

[27] C. J. Tucker, "Red and photographic infrared linear combination for monitoring vegetation," *Remote Sens. Environ.*, vol. 8, no. 2, pp. 127–250, 1979.

[28] N. Strugnell and W. Lucht, "An algorithm to infer continental-scale albedo from AVHRR data, land cover class and field observations of typical BRDFs," *J. Clim.*, vol. 14, no. 7, pp. 1360–1376, Apr. 2001.

[29] W. Lucht and P. Lewis, "Theoretical noise sensitivity of BRDF and albedo retrieval from the EOS-MODIS and MISR sensors with respect to angular sampling," *Int. J. Remote Sens.*, vol. 21, no. 1, pp. 81–98, 2000.

[30] A. Lyapustin, Y. Wang, R. Kahn, J. Xiong, A. Ignatov, R. Wolfe, A. Wu, B. Holben, and C. Brueggc, "Analysis of MODIS-MISR calibration differences using surface albedo around AERONET sites and cloud reflectance," *Remote Sens. Environ.*, vol. 107, no. 1/2, pp. 12–21, 2007.

[31] A. Lyapustin and Y. Wang, "Parameterized code SHARM-3D for radiative transfer over inhomogeneous surfaces," *Appl. Opt.*, vol. 44, no. 35, pp. 7602–7610, Dec. 2005.

[32] W. Lucht, C. B. Schaaf, and A. H. Strahler, "An algorithm for the retrieval of albedo from space using semiempirical BRDF models," *IEEE Trans. Geosci. Remote Sens.*, vol. 38, no. 2, pp. 977–998, Mar. 2000.

Yujie Wang received the B.S. and M.S. degrees in physics from Tsinghua University, Beijing, China, in 1994 and 1998, respectively, and the Ph.D. degree in geography from Boston University, Boston, MA, in 2002.

During his Ph.D. study, his research was mostly focused on the prototyping and validation of the radiative-transfer-based Earth Observing System (EOS) Moderate Resolution Imaging Spectroradiometer (MODIS)/Multiangle Imaging Spectroradiometer (MISR) leaf-area index/fraction of photosynthetically active radiation algorithm. He is currently an Assistant Research Scientist with the Goddard Earth Sciences and Technology Center, University of Maryland, Baltimore County. He is also with the NASA Goddard Space Flight Center, Greenbelt, MD. His research is focused on the radiative transfer of atmosphere, developing a new generic aerosol retrieval and atmospheric-correction algorithm for the EOS MODIS and MISR and the future National Polar Orbiting Environmental Satellite System Visible Infrared Imaging Radiometer Suite instrument.

Alexei I. Lyapustin received the B.S. and M.S. degrees in physics from the Moscow State University, Moscow, Russia, in 1987, and the Ph.D. degree in aerospace remote sensing from the Space Research Institute, Moscow, in 1991.

He is currently an Associate Research Scientist with the Goddard Earth Sciences and Technology Center, University of Maryland, Baltimore County. He is also with the NASA Goddard Space Flight Center, Greenbelt, MD. He actively works in 1-D and 3-D radiative transfer in planetary atmospheres. His research interests are focused on retrievals of atmospheric aerosol and surface bidirectional reflectance from Moderate Resolution Imaging Spectroradiometer (MODIS) and future National Polar Orbiting Environmental Satellite System (NPOESS) Visible Infrared Imaging Radiometer Suite (VIIRS) sensors using time-series analysis. He is a Science Team Member of the MODIS and NPOESS Preparatory Project Science Teams and of the Geostationary Operational Environmental Satellite-R Algorithm Working Group and an Associate Member of the VIIRS Operational Algorithm Team.

Jeffery L. Privette received the B.S. degrees from the University of Michigan, Ann Arbor, and The College of Wooster, Wooster, OH, and the M.S. and Ph.D. degrees from the University of Colorado, Denver, in 1994.

During his tenure with NASA's Goddard Space Flight Center (1996–2006), he held leadership positions in SAFARI 2000, the Moderate Resolution Imaging Spectroradiometer (MODIS) Land Validation Program, and the Committee on Earth Observing Satellites Working Group for Calibration and Validation. He was NASA's Deputy Project Scientist for the National Polar Orbiting Environmental Satellite System (NPOESS) Preparatory Project (NPP) from 2002 to 2006. Since 2006, he has been with the National Climatic Data Center, National Oceanic and Atmospheric Administration Satellite and Information Service, Asheville, NC, where he served as the Project Manager of the Climate Data Record Project. His research has focused on the retrieval and validation of land biophysical parameters from wide field-of-view imagers [e.g., Advanced Very High Resolution Radiometer, MODIS, and Visible Infrared Imaging Radiometer Suite (VIIRS)], with a special emphasis on directional effects. He also serves as the Lead Validation Scientist for NPP Land Products and is a Member of the NPOESS VIIRS Operational Algorithm Team.

Jeffery T. Morisette received the B.A. degree from Siena Heights University, Adrian, MI, the M.S. degree in statistics from Oakland University, Rochester, MI, and the Ph.D. degree from North Carolina State University, Raleigh. He also attended the summer program of the International Space University, Vienna, Austria, in 1996.

Since August 2008, he has been with the U.S. Geological Survey Fort Collins Science Center, Fort Collins, CO, where he serves as the Head of the Invasive Species Science Branch. Before that, he was with the NASA Goddard Space Flight Center for ten years. In Fiscal Year '07, he served a year-long detail at the NASA Headquarters, where he worked in the Applied Science Program. As part of that activity, he became NASA's Policy Liaison to the National Invasive Species Council. His current research is on the application of multiresolution and time-series satellite imagery to ecological and climate studies. Some of his current projects include invasive species habitat mapping in the National Parks and working the U.S. National Phenology Network on land surface phenology research.

Dr. Morisette won the National Oceanic and Atmospheric Administration's National "David Johnson Award for Outstanding Innovative Use of Earth Observation Satellite Data," in 2006.

Brent Holben received the M.S. degree, specializing in biometeorology and remote sensing, from Colorado State University, Fort Collins, in 1976.

He was a Staff Scientist with the Puerto Rico Nuclear Center, University of Puerto Rico, Mayaguez, Puerto Rico, investigating mesoscale radiation balance in the Luquillo Experimental Forest until 1978 when he joined the NASA Goddard Space Flight Center (GSFC), Greenbelt, MD, where he is currently a Research Scientist. He has published on the remote sensing of vegetation dynamics, atmospheric corrections to remotely sensed data, and more recently, aerosol optical properties. He is the Project Leader of the ground-based aerosol characterization program Aerosol Robotic Network, initiating and guiding its development since 1992.